biosensors

MDPI

Article

A Flexible Chemiresistive Sensor Combining Halogen Bonding and Swelling-Mediated Permeation for Field Detection of Plant Stress VOCs

Yu Bai [1], Wei Gan [1,2], Feiyu Chen [1], Ziqin Liao [1,2], Yujie Wu [1,2], Junwei Zheng [1], Kunjie Wang [1], Rui Lin [1], Yuzhu Wang [1], Xiangzeng Kong [1,2] and Xuan Wei [1,*]

[1] College of Mechanical and Electrical Engineering, Fujian Agriculture and Forestry University, Fuzhou 350108, China; 52412048003@fafu.edu.cn (Y.B.); 52412047036@fafu.edu.cn (W.G.); zjw2197540160@163.com (J.Z.); xzkong@fafu.edu.cn (X.K.)
[2] College of Artificial Intelligence, Fujian Agriculture and Forestry University, Fuzhou 350108, China
* Correspondence: xuanwei@fafu.edu.cn

Abstract

Volatile organic compounds (VOCs) act as vital early indicators of biotic or abiotic stress in plants, and their accurate, timely detection is significant for early crop health warning. To address the need for field-deployable sensors with high selectivity, operational stability, and practical usability, we developed a resistive VOC sensor with a sensing layer of 4-fluorothiophenol (FTP)-functionalized silver nanowires embedded in a poly(vinyl alcohol)/poly(3,4-ethylenedioxythiophene)-poly(styrenesulfonate) matrix. Reversible halogen bonding between FTP ligands and aldehyde/ketone groups enables analytes to induce swelling of the PVA matrix, producing significant signal amplification by altering resistance, while aldehydes and ketones are differentiated by polarity and steric hindrance, with optimal responsiveness to aldehydes. The sensor achieves a linear response to aldehydes over 25–200 ppm (R^2 = 0.99), an estimated detection limit of 11.6 ppb, and response and recovery times of ~30 s, with reliable resistance to humidity and temperature variations. Combining stomatal observation with real-time sensor recordings of mechanical damage and pre-symptomatic early blight, we monitored plant stress multidimensionally, detecting disease signals three days before visible symptoms. Principal component analysis establishes stress-type fingerprints, and long short-term memory forecasts VOC emission trends, providing diagnostic classification and predictive intelligence for early intervention and a low-cost, non-destructive pathway for plant health monitoring.

Keywords: chemiresistive sensors; flexible electronics; volatile organic compounds; halogen bonding; plant stress; early warning

Check for updates

Received: 3 September 2026
Revised: 22 September 2026
Accepted: 16 October 2026
Published: 26 October 2026

Copyright: © 2026 by the authors. Licensee MDPI, Basel, Switzerland. This article is an open access article distributed under the terms and conditions of the Creative Commons Attribution (CC BY) license.

1. Introduction

Biotic and abiotic stresses together destroy more than 50% of global crop production each year [1]. Real-time, non-invasive monitoring of plant health is becoming indispensable for protecting crop yield and quality [2]. Visual inspection and computer-vision methods detect problems only post-symptomatically, when pathogens have likely spread and timely intervention is no longer feasible [3]. Diagnostics that report stress before macroscopic signs emerge are therefore urgently needed. Plants under stress actively release characteristic blends of volatile organic compounds (VOCs) into the surrounding air [4]. These emissions act both as chemical signals for plant–environment communication and as indicators of

early stress [5]. Because VOCs are emitted well before visible symptoms develop, their detection affords a valuable pre-symptomatic diagnostic window [6].

In recent years, flexible chemoresistive sensors have shown significant potential for detecting plant VOCs due to their simplicity, low cost, and ease of integration [7,8]. However, the practical application of existing chemiresistive gas sensors is severely constrained by poor selectivity, poor stability, and challenges associated with field deployment [9,10]. Conductive polymers, though flexible and operable at room temperature, typically exhibit low sensitivity and significant baseline noise [11]. Most metal oxide sensors exhibit small differences in their responses to various VOCs and typically require high-temperature operation exceeding 200 °C [12]. Two-dimensional materials such as transition metal dichalcogenides and MXenes enable detection at room temperature but suffer from sluggish recovery kinetics and susceptibility to oxidation-driven degradation under ambient conditions [13]. In real-world deployment, fluctuations in humidity and temperature readily cause signal drift or severe sensitivity attenuation [14,15]. When sensors are mounted on flexible substrates such as plant leaves, they must maintain a stable baseline under mechanical bending [16]. Furthermore, relying on complex algorithms to enhance selectivity and stability substantially increases power consumption and response time, hindering rapid on-site analysis [17,18]. This creates a persistent trade-off reported in existing studies. Materials capable of room-temperature flexible operation typically exhibit poor selectivity and stability, while materials with superior recognition performance often demand high-temperature operation, sophisticated algorithms, or controlled conditions. Therefore, there is an urgent need for a novel flexible chemiresistive sensor that combines high selectivity, robust stability, and suitability for mass production.

In light of the above challenges, this work designs and fabricates a novel composite sensing film that operates via a dual mechanism of halogen-bonding recognition and matrix swelling [19]. The sensing film consists of 4-fluorothiophenol (FTP) ligand-functionalized silver nanowires (AgNWs) embedded in a poly(vinyl alcohol)/poly(3,4-ethylenedioxythiophene)-poly(styrenesulfonate) (PVA/PEDOT:PSS) matrix. FTP acts as the first filtration layer. PVA acts as the second filtration layer. Together, they enable enhanced analyte discrimination without multivariate analysis or array-based pattern recognition. The rationale for the design is that FTP ligands are grafted onto AgNW surfaces via Ag-S bonds. Their terminal fluorine atoms form strong, directional halogen bonds with the carbonyl oxygen of aldehyde and ketone VOCs, enabling specific recognition [20–24]. It also enhances the interactions between these gases and the sensing material. PVA serves as a swellable matrix that expands upon adsorption of target gases, thereby modulating the spacing of the conductive network [25]. PVA further acts as the second filtration layer, modulating the diffusion rate of ketones through steric hindrance and thereby improving overall response specificity. PEDOT:PSS provides an intrinsic conductive pathway and protects the AgNWs from oxidation [26]. Through the synergistic action of these three components, interactions between target gas molecules and the sensing film produce a significant, reversible change in resistance. This design offers the following advantages: (1) higher selectivity than physical adsorption, with the swelling effect amplifying the response and the differential polarity and steric demand of aldehydes versus ketones at the halogen-bonding site and within the PVA phase permitting their discrimination; (2) all-solution processing suited to large-scale, low-cost manufacturing, eliminating vacuum deposition and high-temperature steps; and (3) room-temperature, mechanically and environmentally stable operation appropriate for field deployment. This paper systematically investigates the sensor's material optimization, response characteristics, and environmental adaptability. It demonstrates its application for in situ monitoring and early warning of mechanical damage and early blight disease in tomato leaves.

2. Materials and Methods

2.1. Reagents and Materials

PVA was purchased from Beijing Wokai Biotechnology Co., Ltd., Beijing, China, with a viscosity of 54.0–66.0. PEDOT:PSS was obtained from the Flexible Printed Electronics One-Stop Service Platform, Shenzhen, China, with a solid content of 2–2.5%. Ethanol (99.5%, MW 46.07 g·mol^{-1}), hexanal (97%, MW 100.16 g·mol^{-1}), jasmonic ketone (98%, MW 164.24 g·mol^{-1}), (-)-trans-caryophyllene (98%, MW 204.35 g·mol^{-1}), cis-3-hexenyl acetate (98%, MW 142.20 g·mol^{-1}) and 4-fluorothiophenol (98%, MW 128.17 g·mol^{-1}) were purchased from Shanghai Aladdin Reagent Co., Ltd., Shanghai, China. Dow Corning DC184 polydimethylsiloxane (PDMS) was obtained from Chang'an Songtian Electronic Adhesive Materials Business Department, Dongguan, China. AgNWs were purchased from XFNANO, Nanjing, China, with a diameter of 40 nm and a length of 20–60 µm. All chemicals were used directly without further purification. PI-based flexible interdigitated electrodes were purchased from Xipu Technology, Shenzhen, China, featuring a 100 µm line width and spacing, 10 pairs of 20 fingers, and a finger length of 3.3 mm. Large-fruit tomato seedlings were purchased from Shouhe Seed Industry, Shouguang, China.

2.2. Preparation of Composite Films and PDMS Substrates

First, PVA particles were soaked in deionized water at room temperature for 1 h. Then, a 10 wt.% solution was prepared by heating it in a water bath at 90 °C with continuous stirring [27]. AgNWs (1 mg·mL^{-1}, 1 mL) were mixed with the FTP (10 µM, 100 µL) ligand solution and stirred for 12 h. After centrifugation at 8000 rpm, the mixture was washed three times with deionized water to remove unreacted ligands, yielding FTP-functionalized silver nanowires (FTPAg). Next, PEDOT:PSS (0.5 mL), PVA (10 wt.%, 0.5 mL), and FTPAg (0.25 mL) were combined. The mixture was stirred for 1 h, and then 2 µL was dispensed onto an interdigitated electrode (IDE). It was spun at 1000 rpm to achieve a uniform coating on the IDE surface, followed by drying (Figure 1a). The schematic of the sensor architecture is shown in Figure 1b. To maintain high viscosity before curing during PDMS substrate preparation, the prepolymer and crosslinker were mixed at a 5:1 mass ratio. This delayed the initial formation of the crosslinked network, resulting in higher initial viscosity. The mixture was thoroughly stirred, vacuum degassed, cast into a mold, and cured at 60–70 °C for 2 h to produce the desired elastomer structure. The ductility data for different mixing ratios are shown in Figure S1.

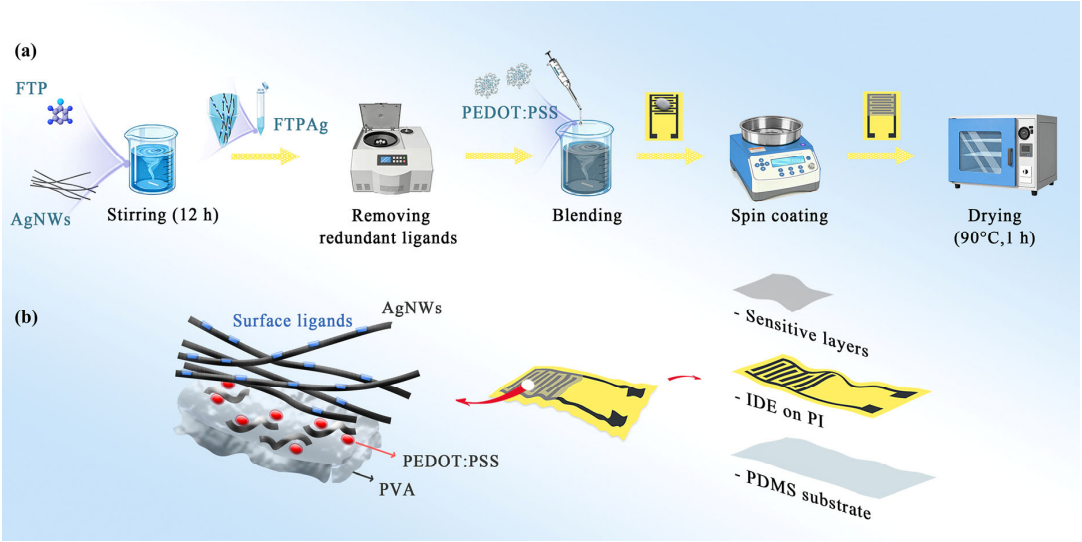


Figure 1. Sensor preparation and structure. (**a**) Sensor preparation workflow. (**b**) Sensor architecture.

2.3. Characterization

The appropriate ligand concentration was measured using a UV–visible spectrophotometer (UV-VIS, UV-600, SHIMADZU, Kyoto, Japan). The morphology and microstructure of the samples were examined using scanning electron microscopy (SEM, Verios G4 UC, Thermo Fisher, Hillsboro, OR, USA). The functional groups and chemical composition of the samples were analyzed by Fourier transform infrared spectroscopy (FTIR, Nicolet iS50, Thermo Fisher, Madison, WI, USA). The water contact angle was measured using an optical contact angle measurement device (JY-82, Dingsheng, Chengde, China). The morphology of FTP-modified AgNWs was examined via transmission electron microscopy (TEM, EM-2100, JEOL Ltd., Akishima, Tokyo, Japan). The surface chemical composition and elemental states of the sensitive film were investigated with X-ray photoelectron spectroscopy (XPS, ESCALAB 250XI, Thermo Fisher Scientific, Waltham, MA, USA). The crystallinity and crystal phase of the sensitive film were determined by X-ray diffraction using Cu Kα radiation of wavelength 1.5406 Å (XRD, D2 PHASER, Bruker, Karlsruhe, Germany). The surface microstructure of the sensitive film was characterized through atomic force microscopy (AFM, MFP-3D, Asylum Research, Santa Barbara, CA, USA).

2.4. Gas Preparation

Static headspace sampling was used. Nitrogen was used as the carrier gas to provide a relatively stable environment for the tested VOCs. In subsequent tests, air was used to purge the VOCs to simulate real application conditions. Target solutions were dispensed into sealed 3L Teflon bags at different volumes, and then the bags were filled with nitrogen to create a calibrated vapor. The sample bags were equilibrated at 25 °C for 8 h [28]. The required volume of test solution at standard atmospheric pressure was calculated using the following equation (Equation (1)).

$$V_s = \frac{cT_0MV}{\omega\rho TV_{m,0}} \quad (1)$$

V_s is the required volume of the test solution (μL), c is the concentration of the test gas in the bag (ppm), T_0 = 273.15 K is the standard temperature, M is the molar mass of the volatile compound (g·mol^{-1}), V is the volume of the gas sampling bag (3 L in this work), ω is the weight fraction purity of the liquid source, ρ is the density of the liquid (g·mL^{-1}), $V_{m,0}$ = 22.4 L·mol^{-1} is the standard molar volume at 273.15 K and 1 atm, and T is the actual preparation temperature (K) [29]. During gas preparation, T is set to 298 K. After reaching equilibrium, pump an equal volume of gas into the gas chamber using a gas pump (Figure S2). Relative humidity in the gas chamber was controlled using a commercial humidifier. The humidifier output was adjusted through feedback control based on the real-time RH reading to maintain the target RH during measurement. Standard sensing tests were performed at 25 °C and 50% relative humidity.

2.5. Sensor Performance Evaluation Methods

The optimization and evaluation considered the following key performance metrics: response amplitude ($\Delta R/R_0$) (Equation (2)), signal-to-noise ratio (SNR) (Equation (3)), response/recovery times, the coefficient of variation (CV) of the response amplitude as key performance metrics (Equation (4)), the limit of detection (LOD) (Equation (5)), and hysteresis (Equation (6)) [30,31].

$$\frac{\Delta R}{R_0} = \frac{R - R_0}{R_0} \quad (2)$$

R is the real-time resistance of the sensor during gas exposure (Ω), and R_0 is the initial baseline resistance of the sensor (Ω). In this work, we report the magnitude of resistance change as a positive response amplitude for intuitive comparison.

The SNR is employed to evaluate the stability and resolvability of the sensor signal.

$$SNR = \frac{S}{N} \tag{3}$$

S is the maximum response resistance (Ω), and N is the standard deviation (SD) of the sensor's resistance values under steady-state conditions in the absence of the target gas. The response and recovery times were defined as the time to reach 90% of the steady-state level [32].

To assess the consistency of the sensor over repeated test cycles, the coefficient of variation (CV) was calculated.

$$CV = \frac{SD_A}{\overline{A}} \tag{4}$$

SD_A is the standard deviation of multiple response amplitude values, and $\overline{A}$ is the mean value of multiple response amplitude values [33].

The LOD was calculated as

$$LOD = \frac{3\sigma}{s} \tag{5}$$

σ is the standard deviation of the response values, and s is the slope of the linear regression equation [34].

Hysteresis was evaluated via the relative residual baseline offset obtained after each VOC–air purge cycle.

$$\Delta_{offset,n} = \frac{R_{0,n+1} - R_{0,n}}{R_{0,n}} \tag{6}$$

$R_{0,n}$ is the average baseline resistance over the steady-state time window before VOC injection in the n-th sensing cycle, and $R_{0,n+1}$ is the average recovered baseline resistance over the steady-state time window after air purging in the n-th cycle. The maximum absolute value of this residual baseline-offset term over repeated cycles is adopted to quantify the hysteresis level of the sensor [35].

2.6. Principal Component Analysis and Long Short-Term Memory Network

Principal Component Analysis (PCA) is used to reduce dimensionality and extract features [36]. It reduces high-dimensional data to a smaller set of principal components via a linear transformation [37]. This method maximizes the preservation of data variability while removing multicollinearity among features, thereby emphasizing the main structure of the data. By statistically reconstructing the original features, PCA enables quantitative characterization and visual differentiation of inherent differences across states or categories [38]. For PCA in this work, three independent biological samples were employed: one healthy plant, one mechanically injured plant, and one plant infected with early blight. Continuous VOC resistive time-series data were acquired over 5 h for each plant and split into 5 hourly segments, generating 15 observational samples in total. As PCA is an unsupervised dimensionality reduction technique, training and test sets were not divided. All observational samples were used for principal component extraction and pattern exploration. For each hourly segment, five metrics were calculated to construct feature vectors: mean, standard deviation (SD), linear slope, area under the curve (AUC), and sample entropy (SampEn). After normalization, these features were fed into a PCA model to identify characteristic patterns of different stress responses. Long Short-Term Memory (LSTM) networks, a specialized type of recurrent neural network, are used for time-series forecasting [39]. With a gated structure that includes forget, input, and output

gates, LSTM selectively memorizes and updates past information, effectively capturing long-term dependencies in the data [40]. A rolling prediction model was built to forecast the next time-step value based on historical resistance sequences, enabling short-term predictions of volatile release trends. The dataset contained 114,461 resistance measurements, which were split chronologically into 70% for training and 30% for testing. The model used 300 historical steps as input and predicted 5 future steps, with 64 LSTM hidden units and a dropout rate of 0.3. Training used the Adam optimizer for 30 epochs with a mini-batch size of 32, an initial learning rate of 0.01, and a gradient threshold of 1. The rolling prediction was then performed recursively for 180 future steps.

2.7. Plant Stress Application and Monitoring Methods

Mechanical injury stress was simulated by making 1 cm cuts on tomato leaves or stems with scissors to replicate physical damage. Sensors were placed near the injury sites for continuous monitoring. Early blight stress was induced by friction inoculation. Once healthy plants showed infection symptoms, healthy leaves were selected to avoid interference from leaf damage caused by manual inoculation [41,42]. To minimize experimental bias caused by inter-individual variation in growth conditions, one representative plant was used for each stress condition. For early blight stress, continuous long-term monitoring was performed on a single leaf to capture the full time course of the response from the pre-symptomatic stage to the symptomatic stage. Sensors continuously monitored volatile changes during the early stages of disease development.

3. Results

3.1. Sensitive Material Optimization and Characterization

3.1.1. Ligand Concentration

Surface modifications were analyzed by ultraviolet–visible (UV-vis) spectroscopy to optimize surface ligand density and content in 2 mL of AgNWs. The FTP ligands were designed to anchor onto AgNW surfaces via thiol–silver self-assembled monolayer chemistry [43]. Before testing, silver nanowires were manually shaken to ensure proper dispersion and prevent breakage. The original solution was diluted sevenfold to keep the optical density within the optimal range, ensuring a complete surface plasmon resonance (SPR) peak shape and clear displacement. The control group consisted of AgNWs dispersed in ethanol at the same concentration without ligand modification. Comparisons showed a significant increase in absorption near 220 nm, consistent with the $\pi \rightarrow \pi^*$ transition characteristic of 4-FTP [44]. The peak around 320 nm primarily reflects the SPR of AgNWs [45]. The sharp spectral profile, with a slight shift, indicates enhanced interaction between the ligands and AgNWs. At 10 μM, changes in absorption peaks were more pronounced, suggesting that ligand modification is most effective at this concentration (Figure 2a). The bond between the ligand and silver nanowires reaches a balanced state—neither too low to affect VOC binding nor too high to cause aggregation and hinder polymerization (Figure S3). We fixed the FTP concentration at 10 μM and tested different volumes. A volume of 200 μL produced the highest and most symmetric peak at 220 nm (Figure 2b). Therefore, we used 200 μL of 10 μM FTP to functionalize 2 mL of AgNWs in subsequent experiments. Finally, the surface chemical state and crystalline phase of the prepared sensitive layer were characterized by XPS and XRD (Figure S4). Fitted C 1s spectra identify multiple carbon chemical states (Figure 2d). The F 1s peak proves stable aromatic C-F bonds of FTP (Figure 2e). The S 2p results confirm Ag-S covalent bonding (~161.38 eV) for FTP ligand immobilization, alongside trace residual thiol (~164.30 eV) and -SO_3H groups (~167–169 eV) from PEDOT:PSS (Figure 2f). All results demonstrate successful fabrication of the composite sensitive layer.

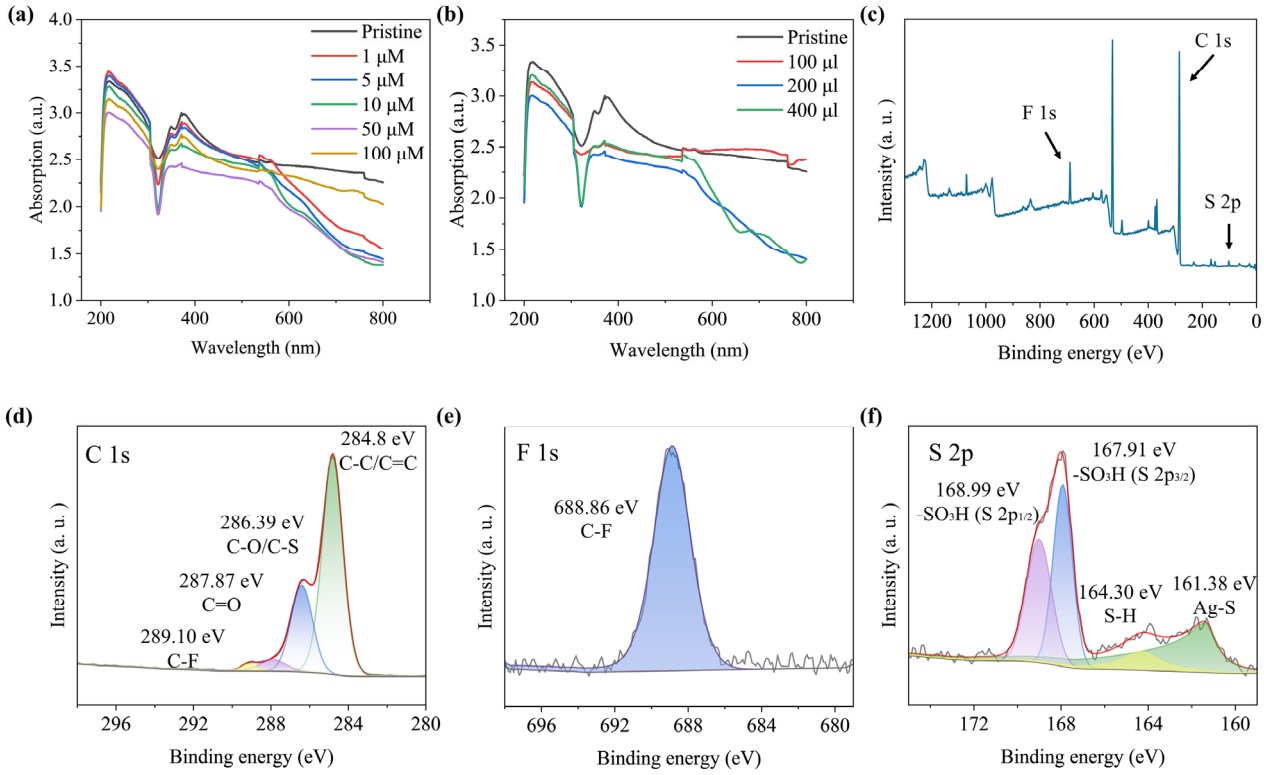


Figure 2. Composition ratio determination and characterization data of the sensitive layer. (**a**) UV-vis data of AgNWs with FTP solutions at different concentrations. (**b**) UV-vis data of AgNWs with varying volumes of FTP solutions. (**c**) Full XPS spectrum, (**d**) C 1s XPS spectrum, (**e**) F 1s XPS spectrum, and (**f**) S 2p XPS spectrum.

3.1.2. PVA Content and Coating Layers

The composition of the sensitive layer plays a decisive role in sensing performance. We first optimized the amount of PVA relative to a fixed amount of FTPAg. To avoid instability caused by excessive AgNW content [46], the amount of PEDOT:PSS was set at twice that of FTPAg. PEDOT:PSS was fixed at 500 μL and FTPAg at 250 μL. The PVA content was then varied, and its effect on sensitivity was tested using 100 ppm hexanal vapor (Figure 3a–e).

Without PVA, hexanal did not elicit a discernible resistance response, and baseline noise was substantial, with a peak-to-peak noise of 5.95 Ω. Adding 250 μL of PVA yielded an SNR of only 7.34, indicating poor stability. With 500 μL of PVA, the SNR increased to 63.68, demonstrating excellent stability. The sensor exhibited a response amplitude of 3.47%, with response and recovery times of 40 s and 23 s, respectively. When the PVA amount was further increased to 750 μL, the response amplitude showed no significant improvement. In contrast, the response and recovery times increased more than fourfold. In some cases, the resistance failed to return to the original baseline. Considering both sensitivity and stability, 500 μL of PVA was determined to be the optimal amount.

Using the optimal PVA volume of 500 μL and a fixed spin-coating speed of 1000 rpm, we controlled film thickness by varying the number of droplet applications. Each application delivered 2 μL of solution. As the number of layers increased, the SNR dropped to 7.93, and the response and recovery times increased substantially. Increasing the number of coating layers from 1 to 2 increased the response amplitude by approximately 2.08%. However, with three layers, the response nearly disappeared (Figure 3f). The two-layer coating exhibited substantial noise, which could cause weak responses to be filtered out as noise in practical applications. This makes two-layer coatings unsuitable for low-concentration detection. Therefore, we selected a single-layer coating. SEM (Figure S5) and AFM (Figure S6) characterizations confirm that the single-layer film exhibits uniform

surface morphology, well-dispersed AgNWs with cold-welded junctions that enhance the conductive network, and a moderate thickness of 16.54 µm (Figure S7), which collectively support the optimal sensing performance observed. To clarify the contributions of FTP and PEDOT:PSS, FTP-free and PEDOT:PSS-free control devices were tested under identical conditions (Figure 4a,b). The results show that removing FTP markedly reduces the selective response to aldehydes/ketones, confirming that FTP is the key recognition unit, while PEDOT:PSS mainly contributes to signal stability rather than molecular recognition. Together with the PVA optimization, these controls help distinguish the roles of the main sensing components.

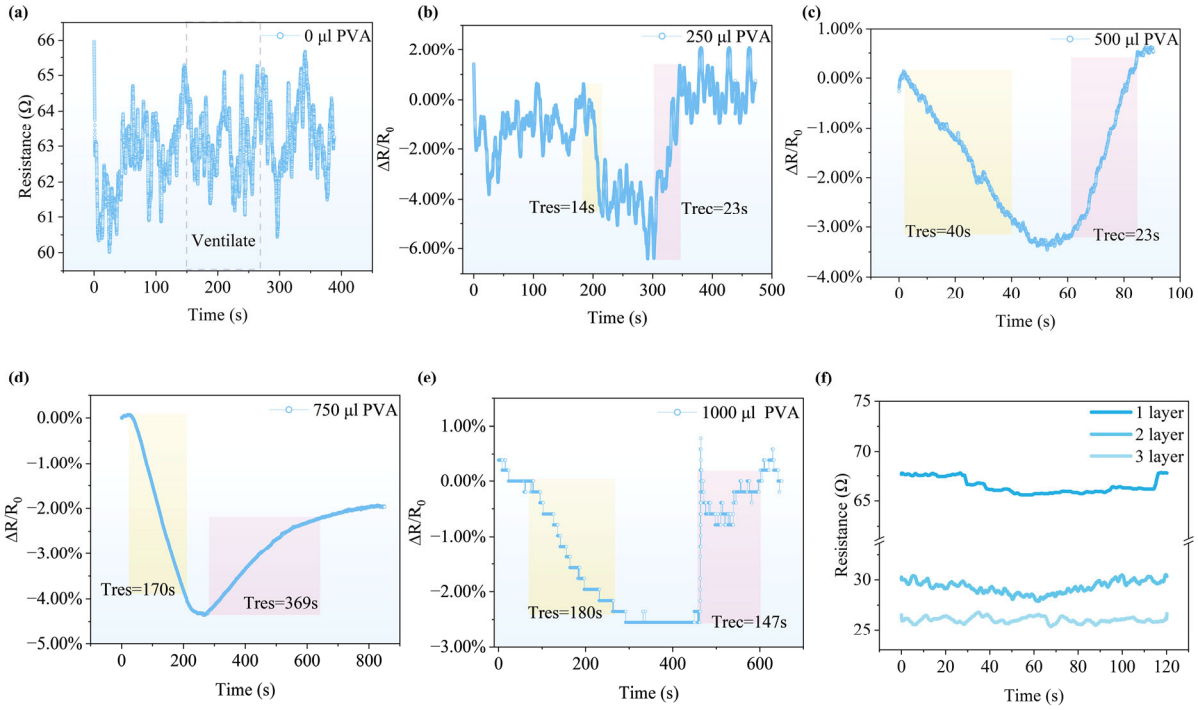


Figure 3. Influence of PVA content and layer number on the sensing performance toward 100 ppm hexanal. (**a**–**e**) Effect of PVA content on readings. (**f**) Effect of the number of sensitive layers on readings.

3.2. Sensor Performance

3.2.1. Selectivity, Repeatability, Environmental Stability, and Bending Stability

The reversible halogen bond formed between halogen atoms and aldehyde groups enables the sensor to selectively recognize aldehyde and ketone compounds [47]. Other common volatile organic compounds were also tested to determine its selectivity [48]. Vapors at identical 100 ppm concentrations, as well as their gas mixtures, were introduced to the same sensor to compare responses. The sensor exhibited almost no response to other gases (Figure 4c). Relative to hexanal, the sensor showed a 0.78% decrease in sensitivity to jasmonic ketone. In terms of response kinetics, the sensor also responded to and recovered from jasmine ketone more slowly, with a response time that was 40 s longer than that for hexanal. Overall, these findings demonstrate that the sensor shows a clear preferential response to aldehydes. (Figure 4d,e).

The sensor's long- and short-term repeatability were assessed using 100 ppm hexanal vapor. After the initial resistance stabilized, clean air was introduced into the gas chamber to purge residual hexanal until the sensor resistance returned to its initial state. The relative standard deviation (RSD) of the response amplitude per cycle was less than 6.7%, indicating good short-term repeatability (Figure 4f). Hysteresis was further quantified using the cyclic

sensing curves. Over repeated cycles, the maximum relative baseline offset was only 1.1%. This offset was attributed to incomplete desorption within the swellable PVA matrix. In subsequent repeatability tests, the findpeaks algorithm was employed to extract the resistance response values for each stimulus. The results showed that, despite baseline drift, the dispersion of responses across cycles remained low (Figure S8).

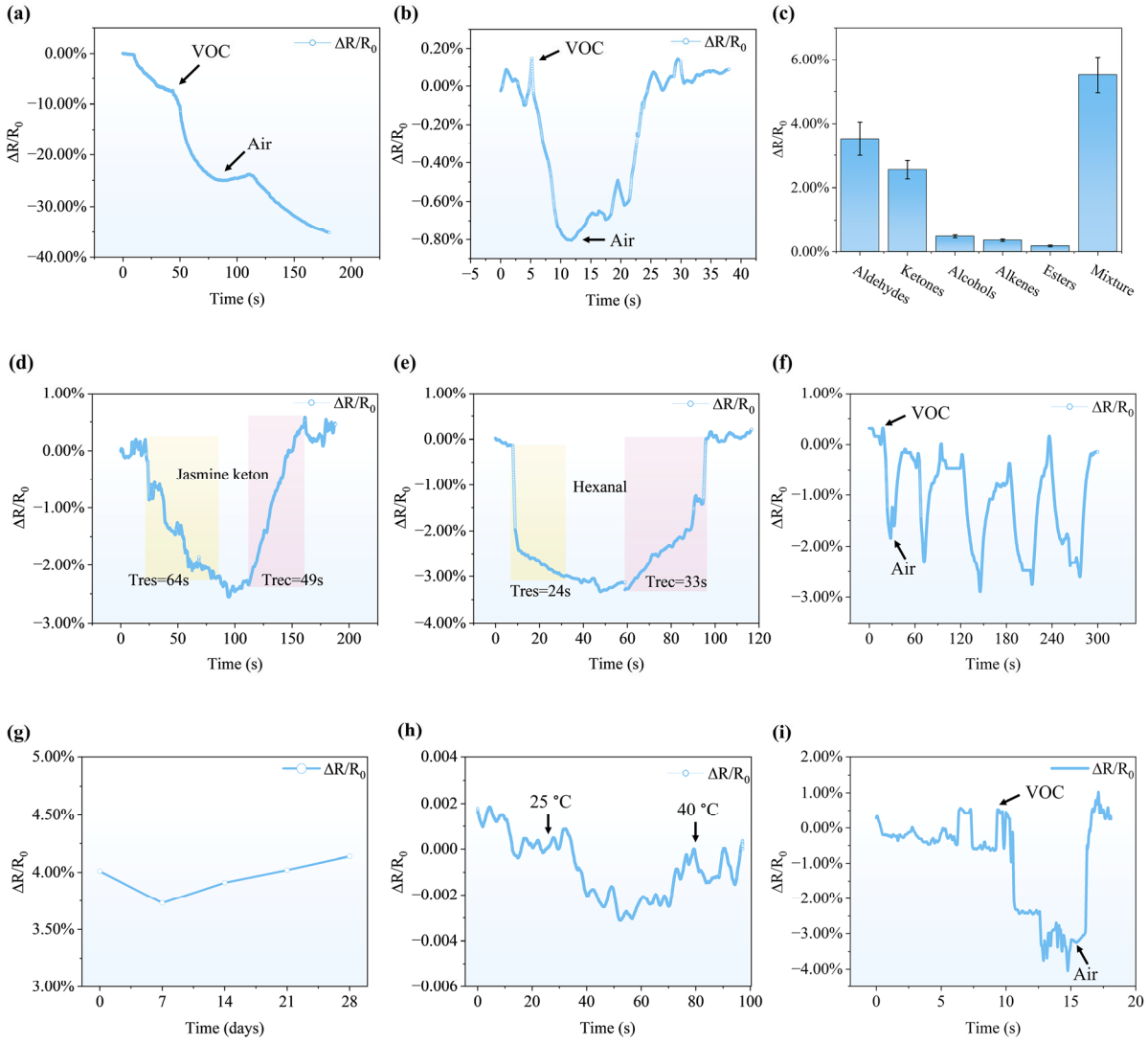


Figure 4. (**a**) FTP-free and (**b**) PEDOT:PSS-free devices to 100 ppm hexanal. (**c**) Sensor response to various VOCs and their gas mixtures. (**d**) Sensor response to 100 ppm jasmone. (**e**) Sensor response to 100 ppm hexanal. (**f**) Short-term repeatability of the sensor. (**g**) Long-term repeatability of the sensor. (**h**) Schematic of temperature-induced baseline drift in the sensor. (**i**) Response of the sensor to 100 ppm hexanal at 90% RH.

Long-term stability testing (Figure S9) shows good repeatability of the response amplitude. The CV was 3.43% over the one-month test (Figure 4g). The baseline resistance fluctuated within ±0.5% during the continuous 15-h test (Figure S10). These results confirm the stability of the chemical and physical structure throughout the test.

Given the typical temperature range for plant growth, resistance data at 25 °C were used as the baseline. The effect of temperature variation from 0 °C to 50 °C on sensor resistance was measured by gradually increasing the temperature from 0 °C and recording resistance changes. Results show that the fractional change in resistance is below 0.005 from 0 °C to 40 °C, and the rate of change increases with temperature (Figure 4h). Resistance fluctuations became more noticeable above 40 °C, with an upward trend, although the

overall temperature impact on the sensor remained insignificant and would not interfere with practical testing of living plants.

Additionally, environmental humidity is a significant interfering factor in practical applications [49]. Dry air was first purged into the chamber. Moisture was then introduced until the RH reached 90%, after which the humidifier switched off automatically. Dry air was purged again. This cycle was repeated to monitor baseline variation. The chamber RH was calibrated and verified with a commercial RH sensor probe. At 90% RH, the sensor's response to 100 ppm hexanal remained unaffected, with only humidity-induced resistance fluctuations observed (Figure 4i). The maximum relative change in resistance due to sensor baseline drift caused by high humidity is only 0.0053. When moisture introduction is stopped, the baseline returns to its initial level (Figure 5a). Results indicate that despite the inherent hydrophilicity of PVA and PEDOT:PSS, the composite sensor fabricated in this study exhibits a water contact angle of 92.7° (Figure 5b) [50]. This surface effectively reduces interference from environmental humidity, preventing disruption by water molecules even at 90% relative humidity.

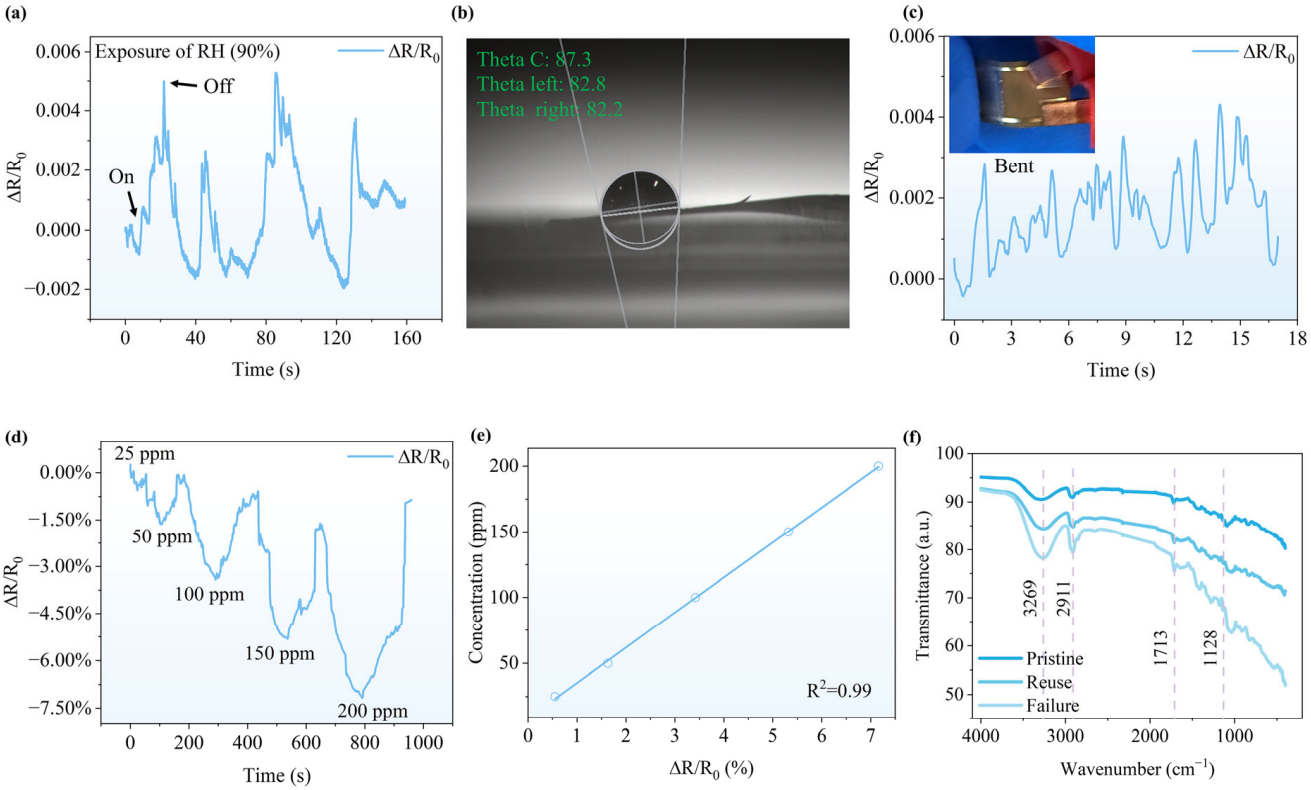


Figure 5. (**a**) Numerical changes under water molecule interference at 90% relative humidity. The "on" and "off" labels denote the on/off states of the commercial humidifier. Dry air was purged simultaneously when the humidifier was switched off. (**b**) Water contact angle of the sensitive layer. (**c**) Effect of bending on sensor readings. (**d**) Sensor response data to different hexanal concentrations. (**e**) Linear relationship of sensor response data to different hexanal concentrations. (**f**) Changes in the FTIR spectrum of the sensitive layer after different testing cycles.

Regarding baseline data fluctuations during polyimide (PI) substrate deformation, the results indicate that the sensor's baseline remains relatively stable under extreme repeated folding conditions. The maximum relative change in baseline resistance is only 0.0043. It also returns to its original level once the external force is removed (Figure 5c).

3.2.2. Sensitivity

Sensor performance was evaluated in hexanal vapor at various concentrations (Figure 5d). When calibrated hexanal vapor at different concentrations was introduced into the gas chamber, the sensor exhibited a strong linear relationship between resistance change and hexanal concentration (Figure 5e) over the range of 25–200 ppm. Linear fitting yields $\Delta R/R = 26.65 \cdot C + 8.62$, with $R^2 > 0.99$. Using this slope and baseline resistance recorded in clean air for 60 s, the LOD was calculated to be 11.6 ppb. The sensor developed in this project demonstrated significantly higher responsiveness than Au@AgNWs and multiwalled carbon nanotubes (MWCNTs) for aldehyde gas detection, exceeding their responses by a factor of three [51]. More comparisons with similar sensors are provided in Table S1 [4,28,52–54].

The pristine, untreated sensitive material, the material after multiple gas exposures, and the degraded or failed material were characterized by FTIR to investigate the fundamental cause of degradation following long-term, repeated testing (Figure 5f). The pristine material and the material exposed multiple times to aldehydes showed consistent peaks for key functional groups. All samples displayed a broad peak at 3269 cm^{-1} corresponding to the hydroxyl–OH group. The peak at 2911 cm^{-1} indicates the stretching vibration of C–H groups in PVA [55]. The peak at 1713 cm^{-1} represents residual acetyl groups in the PVA molecule, while peaks at 1128 cm^{-1} and 1078 cm^{-1} correspond to the –C–O–C–O–C– acetyl group [56,57]. In the fingerprint region (400–500 cm^{-1}), the characteristic vibration peak of the Ag-S bond on the surface of AgNWs remains stable [58]. Notably, no new characteristic peaks appear in the wavenumber range of 1700–1750 cm^{-1} for either material, ruling out irreversible covalent reactions between aldehyde molecules and the sensitive layer [59].

Unlike the previous two cases, the FTIR spectrum of the degraded and failed material clearly shows signs of functional-group destruction. The C-F stretching vibration peak (1100–1250 cm^{-1}) of tetrafluorophenol and the Ag-S bond vibration peak both show significant intensity reduction, indicating that the thiolated surface ligands have detached from the AgNWs. This results in a substantial loss of halogen-bond interaction sites, which are essential for selective recognition. Meanwhile, the O-H stretching vibration peak of PVA shows noticeable broadening and a decrease in intensity, reflecting the disruption of hydrogen bonds between PVA molecular chains. This weakening of hydrogen bonds compromises the substrate's structural integrity, impeding the effective reorganization of the conductive network during swelling-shrinking cycles. The systematic destruction of functional groups directly leads to the sensing material's loss of ability for selective recognition and its physical response to aldehyde gases. This deficiency is the fundamental reason for the failure of detection performance after material degradation.

3.3. In Situ Monitoring and Validation of Plant Stress Responses

The sensor was ultimately attached to tomato leaves to assess its performance. When tomato leaves (Figure 6d) and stems (Figure 6e) were mechanically damaged, sensor resistance rapidly decreased within seconds, with response amplitudes reaching approximately 19.04% (leaf) and 19.59% (stem) (Figure 6a,b). Within 1.14 h after leaf injury, the resistance continued to decline. Then, due to the plant's self-repair process, it reached a peak of 20.48% for a period before starting to increase. Owing to direct severance and incomplete recovery, the stem injury entered an irregular gas-release stage after 2.02 h of self-repair [60]. Experimental data sometimes showed brief spikes above baseline, likely because of the rearrangement of PEDOT:PSS particles after gas exposure. This reorganization temporarily hinders charge transport before stabilization.

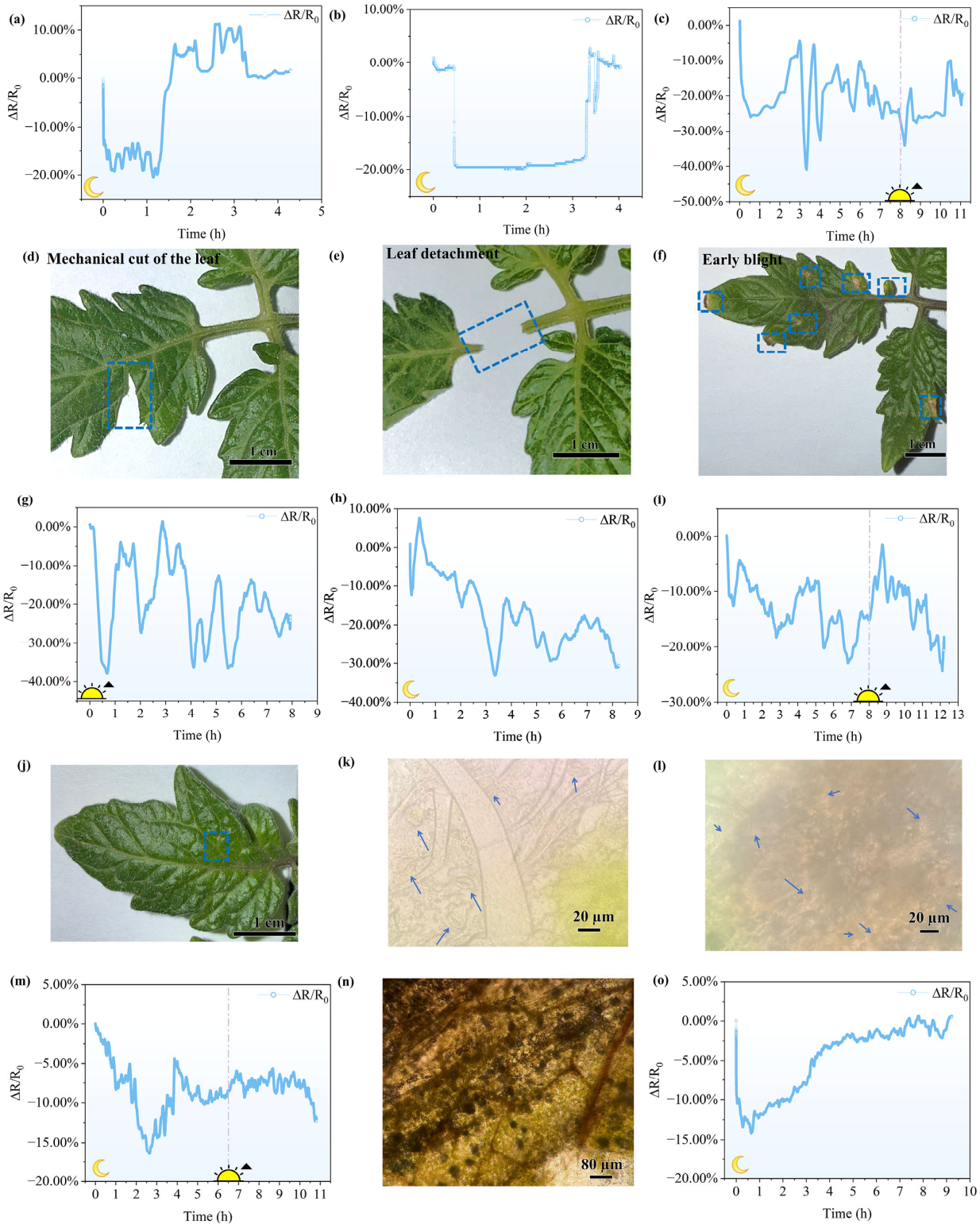


Figure 6. Sensors for plant stress detection. (**a**) Sensor response to mechanical damage on plant leaves. (**b**) Sensor response to mechanical damage on plant stems. (**c**) Sensor response to early blight infection in plants. (**d**) Schematic optical image of mechanical damage on plant leaves. (**e**) Schematic optical image of mechanical damage on plant stems. (**f**) Schematic optical image of early blight infection in plants. (**g**,**h**) Differences in sensor responses to early and late stages of early blight infection. (**i**) Sensor data corresponding to plant early blight as shown in (**j**) after visible disease onset. (**k**) Schematic of stomata in healthy leaves. (**l**) Schematic of stomata in diseased leaves. (**m**) Sensor data corresponding to plant early blight (**n**) after severe visible disease onset. (**o**) Effect of early blight on recovery after mechanical damage to plant leaves.

The sensor enables "preventing disease before it occurs" by detecting early-blight signals three days ahead of symptom appearance. (Figure 6c). The sensor response was much higher than that caused by mechanical damage. The maximum sensor response gradually decreased from 37.93% on day 1 to approximately 22.99% on day 3. When the disease progressed to the level shown in Figure 6f, the response amplitude dropped to 16.42%. This is because, in the early stages of leaf necrosis margins, plants generate new stomata through compensatory mechanisms. However, these newly formed stomata are often unevenly distributed and morphologically abnormal (Figure 6k,l). Over time, leaves develop subtle visible symptoms (Figure 6j). This leads to reduced stomatal conductance and the transmission of stress signals from necrotic to healthy tissue, which trigger non-specific closure of distant stomata and ultimately decrease sensor readings (Figure 6i). This helps farmers detect stress progression. Daytime data, when stomata are open, yield better readings than nighttime data (Figure 6g,h).

At the same time, biological infections can lead to long-term changes in plants. Areas affected by early blight show noticeable necrosis and degeneration (Figure 6n), with dark spots indicating cell death or vacuolar condensation. This structural damage weakens tissue mechanical strength and significantly disrupts physiological functions. After applying the same 1 cm of mechanical damage to infected leaves, comparisons showed slower self-recovery rates, with recovery taking 6.77 h. The response amplitude was 14.17%, which was 6.31% lower than that of healthy plants. Ongoing fluctuations in VOC emissions were also observed (Figure 6o). This occurs because mechanical injury worsens existing flaws, making it more difficult for plants to repair themselves naturally. Simultaneously, disrupted intracellular environments greatly reduce VOC emissions, which are usually released through stomata or epidermal cells, due to decreased synthesis and transport barriers [61].

3.4. Trend Prediction and Pattern Discrimination for Plant Stress

Accurately identifying and predicting stress types from collected data enables timely warnings and improves production management; therefore, this study further developed a resistive time-series analysis framework. The framework first employs an LSTM network to build a rolling prediction model that maps sequences to points (Figure S11). The model achieves high-precision single-step predictions (Figure 7a), with a root mean square error of 0.0007 and a coefficient of determination of 0.9838. It also demonstrates reliable short-term trend extrapolation (Figure 7b), with a correlation coefficient of 0.9597 relative to the actual sequence during 180 consecutive rolling prediction steps. Although the metaheuristic algorithm Particle Swarm Optimization-Backpropagation Algorithm (PSO-BP) from previous work achieves better single-step prediction (R^2 = 0.999, Figure S12), it has high computational resource requirements [62]. For field deployment, LSTM is more suitable and efficient for multi-step prediction. This marks a shift in the early warning system from retrospective real-time alerts to proactive warnings within operational windows.

To further quantify dynamic differences in responses to various stresses and decipher their underlying patterns, PCA was used to extract features and reduce dimensionality from the time-series curves. PCA results showed that the first three principal components collectively explained 99.67% of the variance, corresponding to release intensity and cumulative amount, volatility, and signal complexity, respectively. This approach systematically revealed characteristic "fingerprints" in the response dynamics of early blight, mechanical injury, and healthy plants. This analytical approach not only confirmed the statistical significance of visually observable differences in time-series curves but also provided key indicator-based evidence for early diagnosis. Specifically, it revealed that early blight de-

tection should focus on sustained trend indicators, whereas mechanical damage detection relies more on acute response intensity indicators (Figure 7c).

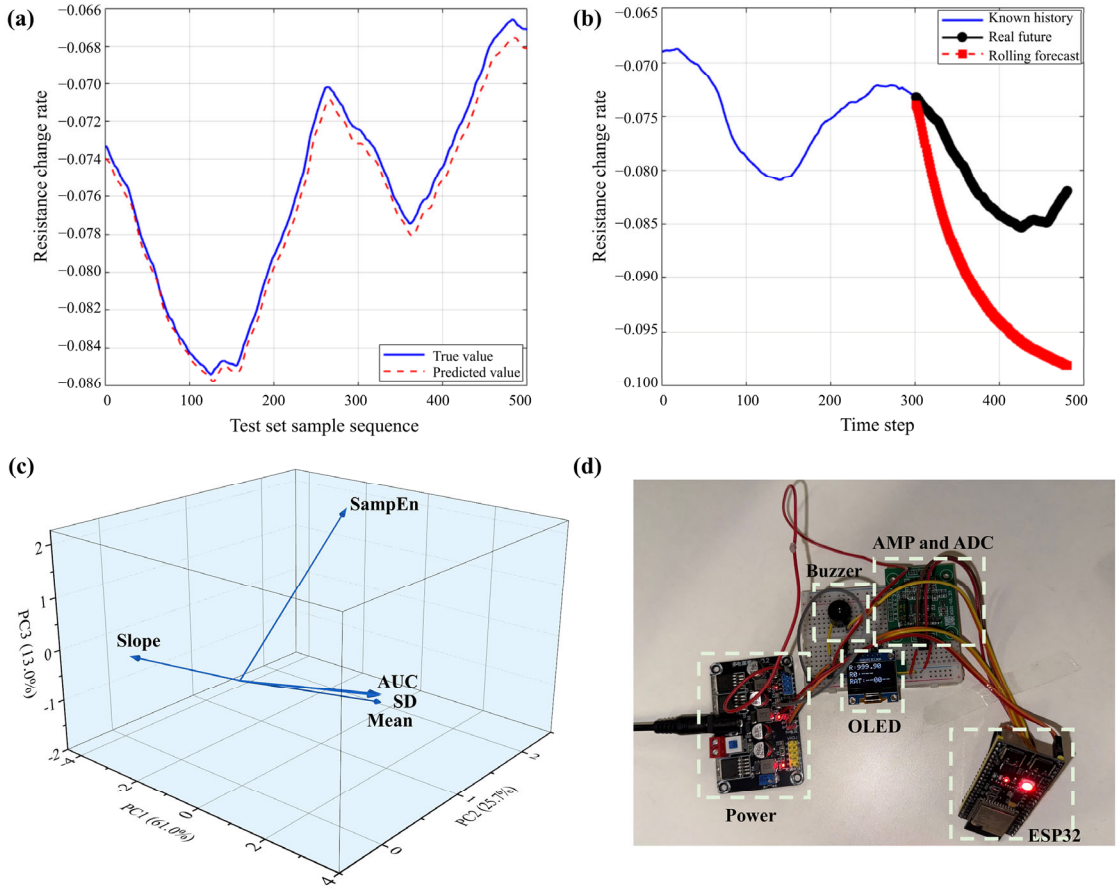


Figure 7. Algorithm application and detection system composition. (**a**) LSTM single-step prediction results. (**b**) LSTM rolling multi-step prediction results. (**c**) PCA loading map. (**d**) Schematic diagram of the embedded alarm system.

Subsequently, we built a comprehensive early warning system (Figure 7d), comprising a resistance sensor, an ESP32 microcontroller, a regulated power supply module, an organic light-emitting diode (OLED) display, and an alarm/button unit. The regulated power supply provides stable voltage to all modules, ensuring system reliability. During operation, the resistance sensor continuously samples the resistance. The analog-to-digital converter (ADC) module converts the analog signal to a digital value and calculates the current resistance. This resistance value can be set as the initial resistance using the buttons, serving as the reference for future comparisons. The system continuously compares the current resistance with the reference resistance. When the preset early warning conditions are met, the ESP32 activates the alarm to signal an abnormal condition. The dynamic process is shown in the video in the Supplemental Materials. Simultaneously, the ESP32 displays real-time resistance values and system status information on the OLED display, allowing users to monitor resistance changes visually.

4. Discussion

4.1. Gas Sensing Mechanism

This study employs swelling-permeation theory [63]. Incorporating silver nanowires that have reacted with thiolated surface ligands in the sensitive layer enables selective detection of molecules containing aldehyde or ketone groups via reversible halogen bonds.

This enhances interactions between the target gas and the sensing material containing halobenzothiophene ligands. The faster response to aldehydes than to ketones arises from their higher polarity and lower steric hindrance, which facilitate both halogen-bond formation and diffusion through the polymer matrix. Exposure to such gases swells the PVA substrate, increasing the distance between conductive nanoparticles [64,65]. During PVA swelling, polymer-chain hydrogen-bond networks loosen, which promotes better contact and charge hopping pathways among PEDOT:PSS conductive phases, ultimately lowering the overall device resistance [66]. This facilitates the redispersion of PEDOT:PSS particles, thereby establishing a more robust conductive network within the composite. This structural reorganization significantly improves charge-transport efficiency, ultimately reducing system resistance. The swelling of PVA is essential to the response, as sensors without PVA show no detectable change. The reversibility of this process is also supported by FTIR analysis, which reveals no new covalent bonds after repeated gas exposure. The use of more electronegative fluorine halogen atoms ensures high detection sensitivity in the sensitive layer (Figure 8) [67].

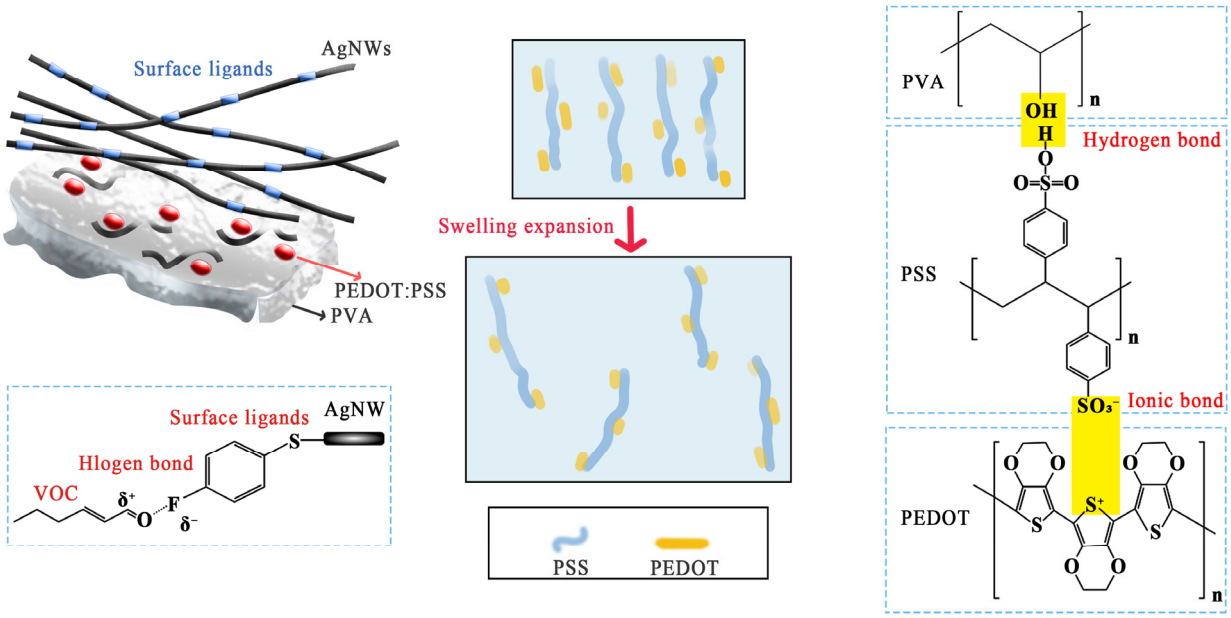


Figure 8. Schematic of sensing principle.

4.2. Sensing Testing

The influence of the sensitive layer composition on sensing performance in this study exhibits a clear trade-off. PVA acts as a double-edged sword in the composite material. Its abundant hydroxyl groups form hydrogen bonds with the Polyvinylpyrrolidone (PVP) layer on the surface of the AgNWs, enhancing interfacial bonding strength [68]. This interaction partially embeds the conductive network within the PVA matrix, providing a structural foundation for the subsequent swelling response [69]. However, excessively high PVA content completely encapsulates the AgNWs, hindering the reversible interaction between gas molecules and the conductive network and causing baseline drift [70]. Experiments determined that 500 µL of PVA is the optimal amount. At this ratio, the sensor maintains both good sensitivity and reversible recovery capability. Simultaneously, the significant influence of the sensitive layer thickness on the response behavior validates the fundamental gas diffusion and adsorption mechanisms in polymer films [71]. It is noteworthy that with a dispensed solution volume of only 2 µL per deposition, slight differences in the actual AgNWs-to-PVA ratio may occur among sensors. These differences can influence gas adsorption efficiency and PVA swelling, representing a key source of inter-sensor

response uncertainty. The optimal response can exceed 4%. Increasing the PVA content reduces the initial resistance but also weakens the magnitude of resistance changes. Optimizing the spin-coating process controls film thickness and uniformity, thereby preventing defects such as coffee rings and pinholes [72]. Control experiments further confirm that the four components act cooperatively: PVA swelling amplifies the signal, FTP provides selective halogen-bonding recognition, AgNWs serve as anchoring sites, and PEDOT:PSS maintains a more stable conductive baseline. The PDMS layer is placed on the back side of the interdigitated electrodes. It does not cover the top sensing film. It acts as a conformal adhesive substrate. This design provides mechanical compliance. It allows the sensor to attach conformally onto uneven leaf surfaces through van der Waals forces. The sensing layer remains fully exposed for VOC interaction. Crucially, this performance is achieved without using expensive noble metals such as gold, resulting in a device cost of less than $2 per unit. This combination of low cost, high stability, and facile fabrication underscores the sensor's strong potential for scalable, real-world deployment in precision agriculture.

Regarding gas recognition selectivity, the sensor shows a stronger response to aldehyde molecules than to ketones. This is because aldehyde groups have higher polarity and form stronger interactions with FTP ligands, as well as experiencing less diffusion due to the greater steric hindrance of ketone molecules [73,74]. When the sensor was exposed to a mixture of five VOCs, each at 100 ppm, the response to the mixture was lower than the sum of the responses to the individual VOCs. This antagonistic behavior suggests that the analytes compete for the finite number of halogen-bonding sites on FTP and for access to the PVA permeation pathways. These results support the conclusion that the sensing response is dominated by specific interactions between FTP and the analytes rather than by the total VOC concentration. FTIR analysis provides crucial evidence for understanding the sensing mechanism. The characteristic functional group peaks in the material after multiple tests closely match those of the original material. This rules out the possibility of irreversible covalent reactions between aldehyde molecules and the sensitive layer [75]. In contrast, the characteristic peaks of C–F, Ag–S, and O–H bonds in degraded materials show significant attenuation. These spectral changes indicate that the detachment of thiolated surface ligands and the disruption of the PVA hydrogen-bond network are the fundamental causes of performance degradation [76,77].

In practical performance validation, the sensor demonstrated excellent environmental adaptability and plant-monitoring capability. The sensing layer exhibited a high water contact angle of 92.7°. This high contact angle is attributed to the migration and enrichment of FTP ligands and the micro/nano-roughness of AgNWs [78,79]. This surface feature restricts water penetration into the intrinsically hydrophilic and swellable PVA matrix, thereby suppressing humidity-induced swelling and its interference with sensing, and enabling stable operation even at 90% RH [80]. Temperature-induced baseline drift remained negligible and controllable within 0–40 °C. Fluctuations above 40 °C primarily stemmed from external circuitry rather than from the sensing layer itself, thereby meeting monitoring requirements across plant growth temperature ranges [81]. Overall, the baseline drift observed under temperature, humidity, and bending is small and reversible. It mainly originates from external environmental/mechanical perturbations rather than from irreversible degradation of the sensing layer or instability of the measurement setup. The residual noise is associated with the reversible rearrangement of the PEDOT:PSS conductive network and humidity feedback control. This does not compromise the sensor's practical stability [82]. In Situ testing on tomato plants demonstrated the sensor's ability to capture subtle variations in plant physiological states. It responded immediately to mechanical damage, provided a three-day early warning of early blight infection, and enabled monitoring of recovery capacity in infected plants after secondary damage. Notably, the sensor's daily response

patterns correlated strongly with stomatal behavior, suggesting it not only detects volatile emissions but may also indirectly reflect plant stomatal regulation rhythms. This offers a new observational approach for understanding plant-environment interactions.

The introduction of data-driven methods enables a shift from qualitative to quantitative analysis in plant stress monitoring [83,84]. The LSTM time-series prediction model provides high-precision single-step forecasts and reliable multi-step extrapolations, transforming early warning systems from retrospective real-time alerts into proactive alerts within operational windows. PCA feature extraction further reveals characteristic fingerprints in the response dynamics of different stress types. This ability to recognize quantitative features, combined with embedded early warning systems, upgrades sensors from simple signal converters to intelligent monitoring terminals with analytical capabilities. This offers a practical technical pathway for non-destructive plant health monitoring in future agricultural Internet of Things applications.

5. Conclusions

This study developed a flexible chemoresistive sensor that detects plant-emitted VOCs through synergistic interplay of halogen-bonding recognition and polymer-matrix swelling, enabling real-time and pre-symptomatic monitoring of plant stress. By optimizing ligand concentration, swellable polymers, PVA content, and coating processes, a highly sensitive layer with fast response, good selectivity, and excellent stability was achieved. The material cost of below $2 per unit makes it suitable for mass production. The sensor achieves an estimated detection limit of 11.6 ppb for hexanal, with a linear range of 25–200 ppm and response/recovery times of 40 s and 23 s, respectively. Short-term repeated cycles show an RSD below 6.7% and a maximum relative baseline offset of only 1.1%. Long-term testing gives a CV of 3.43% over four weeks. It remains stable under 90% RH and high humidity, and after repeated extreme bending cycles. In field plant monitoring, the sensor successfully issued warnings for mechanical damage and early blight; furthermore, by combining LSTM and PCA to analyze data on early-stage symptomatic plant stress, the feature fingerprint profiles and predicted stress trends were obtained, which will help improve the timeliness and specificity of stress responses in agricultural practice. We also developed an intelligent detection system that provides a real-time, low-cost, and non-destructive way to monitor plant health, offering great promise for broad application in the agricultural sector.

Supplementary Materials: The following supporting information can be downloaded at https://www.mdpi.com/article/10.3390/bios16110607/s1. Figure S1: the ductility data of PDMS prepolymer and curing agent at different ratios; Figure S2: schematic of experimental setup for gas sensing measurements; Figure S3: TEM image of FTP-modified AgNWs; Figure S4: XRD comparison of pure PVA and the fabricated sensitive layer; Figure S5: SEM characterization of AgNWs-loaded PVA/PEDOT:PSS and schematic of cold welding; Figure S6: AFM height images of the sensitive layer; Figure S7: single layer coating cross-sectional thickness; Figure S8: repeatability performance of the sensor; Figure S9: long-term sensitivity data of the sensor within four weeks; Figure S10: long-term baseline stability test results over time; Figure S11: Establishing an LSTM rolling prediction model from sequence to point; Figure S12: Single-step prediction results of the PSO-BP model; Table S1: comparison of gas sensing performance for plant volatile organic compounds; Video S1: sensor system alarm triggered by mechanical damage to plants.

Author Contributions: Conceptualization, Y.B. and X.W.; methodology, Y.B., W.G., R.L. and Z.L.; software, W.G., J.Z., Y.W. (Yuzhu Wang) and K.W.; validation, F.C. and Y.B.; formal analysis, Y.B., W.G. and Z.L.; investigation, Y.B.; resources, X.K. and X.W.; data curation, W.G. and F.C.; writing—original draft preparation, Y.B., Y.W. (Yujie Wu) and X.W.; writing—review and editing, all authors; visualization, Y.B. and Y.W. (Yujie Wu); supervision, X.W.; project administration, X.W.; funding acquisition, X.K. and X.W.; J.Z., K.W. and Y.W. (Yuzhu Wang) jointly carried out all the circuit design,

component selection, programming, and application testing for the subsequent sensor applications; X.K. and X.W. not only provided financial support and subsequent content review but also offered many valuable suggestions for improvement, ensuring the smooth progress of the project. All authors have read and agreed to the published version of the manuscript.

Funding: The authors gratefully acknowledge the financial support provided by the National Natural Science Foundation of China (No. 32672536), Fujian Agriculture and Forestry University Science and Technology Innovation Special Fund project (KFB25034A).

Institutional Review Board Statement: Not applicable.

Informed Consent Statement: Not applicable.

Data Availability Statement: The raw data supporting the conclusions of this article will be made available by the authors on request.

Acknowledgments: During the preparation of this manuscript, the authors used DeepSeek-V4, a large language model, during manuscript revision to assist with language polishing, primarily to improve grammar, wording, sentence fluency, and the naturalness of academic English. Importantly, DeepSeek-V4 was used solely for language-related improvements. It was not used to generate research data, conduct statistical analyses, interpret the findings, or formulate the study conclusions. All AI-assisted revisions were carefully reviewed, edited, and approved by the authors, who remain fully responsible for the accuracy and integrity of the manuscript.

Conflicts of Interest: The authors declare no conflicts of interest.

Abbreviations

The following abbreviations are used in this manuscript:

VOCs	volatile organic compounds
RH	relative humidity
FTP	4-fluorothiophenol
AgNWs	silver nanowires
PVA	poly(vinyl alcohol)
PEDOT:PSS	poly(3,4-ethylenedioxythiophene):poly(styrenesulfonate)
PDMS	polydimethylsiloxane
FTPAg	FTP-functionalized silver nanowires
IDE	interdigitated electrode
UV-vis	ultraviolet–visible spectrophotometer
SEM	scanning electron microscopy
FTIR	Fourier transform infrared spectroscopy
TEM	transmission electron microscopy
XPS	X-ray photoelectron spectroscopy
XRD	X-ray diffraction
AFM	atomic force microscopy
PCA	Principal Component Analysis
LSTM	Long Short-Term Memory
SPR	surface plasmon resonance
SNR	signal-to-noise ratio
SD	standard deviation
PI	Polyimide

References

1. Gbiliy, A.; Senosy, I.; Saadan, M.A.A.; Di, X.; Sayed, M.; Gao, Y.-Y.; Liao, P.; Kandegama, W.M.W.W.; Wang, M.-Q.; Hao, G.-F. Nanoarchitectures-Powered Volatile Organic Compound Sensors Enable Real-Time Monitoring and Early Warning in Sustainable Agriculture. *Coord. Chem. Rev.* **2026**, *548*, 217169. [CrossRef]

2. Park, H.; Han, J.; Myoung, S.; Kim, M.; Lim, H.; Kim, D.; Lee, G. Non-Invasive Wearable Sensors for Monitoring Plant Health. *Macromol. Res.* **2025**, *33*, 691–702. [CrossRef]
3. Rezaei, M.; Diepeveen, D.; Laga, H.; Jones, M.G.K.; Sohel, F. Plant Disease Recognition in a Low Data Scenario Using Few-Shot Learning. *Comput. Electron. Agric.* **2024**, *219*, 108812. [CrossRef]
4. Sangmen, E.D.; Solaiman, M.; Sarker, T.C.; Galib, A.R.; Inam, A.K.M.S.; Somenahally, A.C.; Tabassum, S. An Integrated Methanol and Terpene Sensing Platform for Real-Time VOC Profiling of Nitrogen-Stressed Cotton Plants. *Comput. Electron. Agric.* **2026**, *245*, 111569. [CrossRef]
5. Ogwu, M.C.; Ulimboka, R.; Aliu, O.O. Decoding Plant Volatile Stress Signals across Scales: From Molecular Responses to Ecosystem Dynamics. *Front. Plant Sci.* **2026**, *17*, 1815183. [CrossRef] [PubMed]
6. Hernández, I.; Gutiérrez, S.; Barrio, I.; Íñiguez, R.; Tardaguila, J. In-Field Disease Symptom Detection and Localisation Using Explainable Deep Learning: Use Case for Downy Mildew in Grapevine. *Comput. Electron. Agric.* **2024**, *226*, 109478. [CrossRef]
7. Guo, Y. Wearable Sensors to Monitor Plant Health. *Nat. Food* **2023**, *4*, 350. [CrossRef] [PubMed]
8. Reddy, B.K.S.; Borse, P.H. Review—Recent Material Advances and Their Mechanistic Approaches for Room Temperature Chemiresistive Gas Sensors. *J. Electrochem. Soc.* **2021**, *168*, 057521. [CrossRef]
9. Turlybekuly, A.; Shynybekov, Y.; Soltabayev, B.; Yergaliuly, G.; Mentbayeva, A. The Cross-Sensitivity of Chemiresistive Gas Sensors: Nature, Methods, and Peculiarities: A Systematic Review. *ACS Sens.* **2024**, *9*, 6358–6371. [CrossRef] [PubMed]
10. Bulemo, P.M.; Kim, D.-H.; Shin, H.; Cho, H.-J.; Koo, W.-T.; Choi, S.-J.; Park, C.; Ahn, J.; Güntner, A.T.; Penner, R.M.; et al. Selectivity in Chemiresistive Gas Sensors: Strategies and Challenges. *Chem. Rev.* **2025**, *125*, 4111–4183. [CrossRef] [PubMed]
11. Yan, Y.; Yang, G.; Xu, J.-L.; Zhang, M.; Kuo, C.-C.; Wang, S.-D. Conducting Polymer-Inorganic Nanocomposite-Based Gas Sensors: A Review. *Sci. Technol. Adv. Mater.* **2020**, *21*, 768–786. [CrossRef] [PubMed]
12. Lian, M.; Luan, K.; He, T.; Chen, D. Rational Design of $NiCo_2O_4/Ti_3C_2$ MXene Heterostructure for Unmanned Aerial Vehicles-Enabled Real-Time CO Monitoring. *ACS Sens.* **2025**, *10*, 6241–6252. [CrossRef] [PubMed]
13. Qian, L.; Rahmati, F.; Li, F.; Zhang, T.; Wang, T.; Zhang, H.; Yan, S.; Zheng, Y. Recent Advances in 2D MXene-Based Heterostructures for Gas Sensing: Mechanisms and Applications in Environmental and Biomedical Fields. *Nanoscale* **2025**, *17*, 8975–8998. [CrossRef] [PubMed]
14. Peng, B.; Wu, X.; Zhang, C.; Zhang, C.; Lan, L.; Ping, J.; Ying, Y. In-Time Detection of Plant Water Status Change by Self-Adhesive, Water-Proof, and Gas-Permeable Electrodes. *ACS Appl. Mater. Interfaces* **2023**, *15*, 19199–19208. [CrossRef] [PubMed]
15. Lee, S.; Kim, J.; Kim, D.; Park, H.; Myoung, S.; Han, J.; Park, C.; Kim, Y.; Choi, C.; Lee, G. Wearable Volatile Organic Compound Sensors for Plant Health Monitoring. *Adv. Sustain. Syst.* **2024**, *8*, 2300634. [CrossRef]
16. Yun, J.; Cho, M.; Lee, K.; Kang, M.; Park, I. A Review of Nanostructure-Based Gas Sensors in a Power Consumption Perspective. *Sens. Actuators B Chem.* **2022**, *372*, 132612. [CrossRef]
17. Conti, P.P.; Iacomi, P.; Nicolas, M.; Maurin, G.; Devautour-Vinot, S. MIL-101(Cr)@QCM and MIL-101(Cr)@IDE as Sorbent-Based Humidity Sensors for Indoor Air Monitoring. *ACS Appl. Mater. Interfaces* **2023**, *15*, 33675–33681. [CrossRef] [PubMed]
18. Wang, X.; Qi, H.; Shao, Y.; Zhao, M.; Chen, H.; Chen, Y.; Ying, Y.; Wang, Y. Extrusion Printing of Surface-Functionalized Metal-Organic Framework Inks for a High-Performance Wearable Volatile Organic Compound Sensor. *Adv. Sci.* **2024**, *11*, 2400207. [CrossRef] [PubMed]
19. Weis, J.G.; Ravnsbæk, J.B.; Mirica, K.A.; Swager, T.M. Employing Halogen Bonding Interactions in Chemiresistive Gas Sensors. *ACS Sens.* **2016**, *1*, 115–119. [CrossRef]
20. Arndt, T.; Ghazi Zahedi, H.; Breugst, M. Carbonyl-Alkyne Metathesis Reactions Catalyzed by Organic Halogen-Bond Donors. *Eur. J. Org. Chem.* **2024**, *27*, e202400595. [CrossRef]
21. Damrath, M.; Döring, A.; Nachtsheim, B.J. Halogen Bond-Catalyzed Pictet–Spengler Reaction. *Chem. Commun.* **2025**, *61*, 4828–4831. [CrossRef] [PubMed]
22. Sysoeva, A.A.; Safinskaya, Y.V.; Il'in, M.V.; Novikov, A.S.; Bolotin, D.S. Halonium and Chalconium Salt-Catalyzed Schiff Condensation: Kinetics and DFT Insights into Organocatalyst Activity Parameters. *Org. Biomol. Chem.* **2025**, *23*, 1970–1980. [CrossRef] [PubMed]
23. Galathri, E.M.; Tsampalis, K.; Kuczmera, T.J.; Tzeli, D.; Nachtsheim, B.J.; Kokotos, C.G. Organocatalytic Acetalization of Aldehydes Utilizing N-Heterocyclic Iod(Az)Olium Salts as the Halogen-Bonding Catalysts. *ChemCatChem* **2026**, *18*, e01549. [CrossRef]
24. Vonnemann, C.J.; Engelage, E.; Ward, J.S.; Rissanen, K.; Keller, S.; Huber, S.M. *Ortho*-Carborane-Derived Halogen Bonding Organocatalysts. *Angew. Chem. Int. Ed.* **2025**, *64*, e202424072. [CrossRef] [PubMed]
25. Lv, C.; Zhou, X.; Chen, C.; Liu, X.; Qian, J. Highly Sensitive and Flexible Ammonia Sensor Based on PEDOT:PSS Doped with Lewis Acid for Wireless Food Monitoring. *Chem. Eng. J.* **2024**, *493*, 152652. [CrossRef]
26. Karagiorgis, X.; Shakthivel, D.; Khandelwal, G.; Ginesi, R.; Skabara, P.J.; Dahiya, R. Highly Conductive PEDOT:PSS: Ag Nanowire-Based Nanofibers for Transparent Flexible Electronics. *ACS Appl. Mater. Interfaces* **2024**, *16*, 19551–19562. [CrossRef] [PubMed]

27. Thomas, L.M.; Sreekanth, M.S. Enhanced Water-Induced Shape Memory and Swelling Characteristics of Graphene Oxide-Cellulose Nanofiber Reinforced Polyvinyl Alcohol Nanocomposites. *J. Vinyl Addit. Technol.* **2025**, *31*, 728–755. [CrossRef]
28. Zheng, C.; Zhou, Q.; Wang, J.; Du, D. Wireless Plant Stresses Monitoring with a Wearable Chemiresistor Gas Sensor at Room Temperature. *Sens. Actuators B Chem.* **2023**, *381*, 133408. [CrossRef]
29. Zhou, Q.; Zheng, C.; Zhu, L.; Wang, J. Tin Sulfides Heterostructure Modified Quartz Crystal Microbalance Sensors with High Sensitivity for Hazardous Trimethylamine Gas. *Sens. Actuators B Chem.* **2022**, *371*, 132520. [CrossRef]
30. Wang, H.; Ogolla, C.O.; Panchal, G.; Hepp, M.; Delacroix, S.; Cruz, D.; Kojda, D.; Ciston, J.; Ophus, C.; Knop-Gericke, A.; et al. Flexible CO_2 Sensor Architecture with Selective Nitrogen Functionalities by One-Step Laser-Induced Conversion of Versatile Organic Ink. *Adv. Funct. Mater.* **2022**, *32*, 2207406. [CrossRef]
31. Shin, W.; Hong, S.; Jeong, Y.; Jung, G.; Park, J.; Kim, D.; Choi, K.; Shin, H.; Koo, R.-H.; Kim, J.-J.; et al. Low-Frequency Noise in Gas Sensors: A Review. *Sens. Actuators B Chem.* **2023**, *383*, 133551. [CrossRef]
32. Sharma, A.; Mahajan, A. Potential Applications of Chemiresistive Gas Sensors. In *Carbon Nanomaterials and Their Nanocomposite-Based Chemiresistive Gas Sensors*; Elsevier: Amsterdam, The Netherlands, 2023; p. 223.
33. Xu, R.; Beltrán-Gutiérrez, R.E.; Käding, M.; Lange, A.; Marx, S.; Ostermann, J. Frequency Dependent Amplitude Response of Different Couplant Materials for Mounting Piezoelectric Sensors. *NDT E Int.* **2024**, *141*, 102993. [CrossRef]
34. Guo, Y.; Feng, H.; Zhao, Q.; Guo, S.; Ou, R.; Zhang, S.; Duan, Z.; Xia, Y.; Yuan, Z.; Hou, M.; et al. Highly Selective NO_2 Sensing for *m*Obile on-Site Monitoring Enabled by a Dual-Sensitization Mechanism in Palladium Sulfide-Based Nanocomposites. *Chem. Eng. J.* **2026**, *546*, 179922. [CrossRef]
35. Kumar, Y.; Sharma, A.; Shirage, P.M. Shape-Controlled $CoFe_2O_4$ Nanoparticles as an Excellent Material for Humidity Sensing. *RSC Adv.* **2017**, *7*, 55778–55785. [CrossRef]
36. Ayesha, S.; Hanif, M.K.; Talib, R. Overview and Comparative Study of Dimensionality Reduction Techniques for High Dimensional Data. *Inf. Fusion* **2020**, *59*, 44–58. [CrossRef]
37. Mei, H.; Peng, J.; Wang, T.; Zhang, B.; Xuan, F.; Wang, L.; Zeng, M.; Yang, Z. Smart VOCs Recognition System Based on Single Gas Sensor and Multi-Task Deep Learning Model. *Sens. Actuators B Chem.* **2025**, *439*, 137853. [CrossRef]
38. Wold, S.; Esbensen, K.; Geladi, P. Principal Component Analysis. *Chemom. Intell. Lab. Syst.* **1987**, *2*, 37–52. [CrossRef]
39. Hochreiter, S.; Schmidhuber, J. Long Short-Term Memory. *Neural Comput.* **1997**, *9*, 1735–1780. [CrossRef] [PubMed]
40. Gers, F.A.; Schmidhuber, J.; Cummins, F. Learning to Forget: Continual Prediction with LSTM. In Proceedings of the 1999 Ninth International Conference on Artificial Neural Networks ICANN 99 (Conf. Publ. No. 470), Edinburgh, UK, 7–10 September 1999; Volume 2, pp. 850–855.
41. Ameye, M.; Allmann, S.; Verwaeren, J.; Smagghe, G.; Haesaert, G.; Schuurink, R.C.; Audenaert, K. Green Leaf Volatile Production by Plants: A Meta-Analysis. *New Phytol.* **2018**, *220*, 666–683. [CrossRef] [PubMed]
42. Heil, M.; Silva Bueno, J.C. Within-Plant Signaling by Volatiles Leads to Induction and Priming of an Indirect Plant Defense in Nature. *Proc. Natl. Acad. Sci. USA* **2007**, *104*, 5467–5472. [CrossRef] [PubMed]
43. Han, S.; Li, P.; Sun, X.; Sun, F. VOC Biomarker-Based Wearable Gas Sensors for Real-Time in Situ Monitoring of Plant Stress and Health: Applications and Technical Barriers. *Front. Plant Sci.* **2026**, *17*, 1909243. [CrossRef] [PubMed]
44. Liu, X.; Ki, T.; Deng, G.; Yoo, S.; Lee, K.; Lee, B.-H.; Hyeon, T.; Bootharaju, M.S. Recent Advances in Synthesis and Properties of Silver Nanoclusters. *Nanoscale* **2024**, *16*, 12329–12344. [CrossRef] [PubMed]
45. Zhang, B.; Lin, X.; Li, J.; Xu, X.; Xie, J.; Wang, Q.; Ma, R.; Mo, Z.; Xu, X.; Xu, H. Enhanced Photocatalytic Disinfection with Surface Plasmon Resonance Effect in S-Scheme Heterojunction. *Sol. Energy* **2026**, *306*, 114321. [CrossRef]
46. Dcosta, J.V.; Ochoa, D.; Sanaur, S. Extensive Properties Investigation of AgNWs-PEDOT:PSS Based Transparent Conductive Electrode for Ultraflexible Organic Photodetector Applications. *Adv. Electron. Mater.* **2024**, *10*, 2300559. [CrossRef]
47. Taylor, A.J.; Hein, R.; Patrick, S.C.; Davis, J.J.; Beer, P.D. Anion Sensing through Redox-Modulated Fluorescent Halogen Bonding and Hydrogen Bonding Hosts. *Angew. Chem. Int. Ed.* **2024**, *63*, e202315959. [CrossRef] [PubMed]
48. Liu, X.; Fan, P.; Jiang, J.; Gao, Y.; Liu, C.; Li, S.; Liang, Z. Evolution of Volatile Compounds Composition during Grape Berry Development at the Germplasm Level. *Sci. Hortic.* **2022**, *293*, 110669. [CrossRef]
49. Vadera, N.; Dhanekar, S. Classification and Prediction of VOCs Using an IoT-Enabled Electronic Nose System-Based Lab Prototype for Breath Sensing Applications. *ACS Sens.* **2024**, *10*, 439–447. [CrossRef] [PubMed]
50. Chen, Z.-C.; Chang, T.-L.; Lee, H.-S.; Fan, J.-Y.; Wang, C.-P. Investigation into Anti-Dust Wetting Surface with Coral-like Nanostructures Reinforced by Electrospun Composite Nanofibers. *Int. J. Adv. Manuf. Technol.* **2022**, *118*, 2601–2612. [CrossRef]
51. Lee, G.; Hossain, O.; Jamalzadegan, S.; Liu, Y.; Wang, H.; Saville, A.C.; Shymanovich, T.; Paul, R.; Rotenberg, D.; Whitfield, A.E.; et al. Abaxial Leaf Surface-Mounted Multimodal Wearable Sensor for Continuous Plant Physiology Monitoring. *Sci. Adv.* **2023**, *9*, eade2232. [CrossRef] [PubMed]
52. Yang, B.; Thi Hanh To, D.; Sobolak, D.; Mendoza, E.R.; Myung, N.V. High Performance Methyl Salicylate Gas Sensor Based on Noble Metal (Au, Pt) Decorated WO_3 Nanofibers. *Sens. Actuators B Chem.* **2024**, *413*, 135741. [CrossRef]

53. Singh, R.; Kulkarni, S.; Ghosh, R. Nickel Oxide Nanoflowers Based Resistive Sensors for Detecting Methyl Salicylate and Linalool. *Phys. Scr.* **2025**, *100*, 015045. [CrossRef]
54. Jaishi, L.R.; Ding, W.; Yuan, J.; Anas, M.; Kharel, P.; Xian, X. Piezoelectric–Optical Hybrid Sensor for Trace-Level Detection of (E)-2-Hexenal via Tuned Zn–Co/ZIF-8 Frameworks for Plant Health Monitoring. *ACS Sens.* **2025**, *10*, 6623–6633. [CrossRef] [PubMed]
55. Mitani, E.; Ozaki, Y.; Sato, H. Two Types of CO· · · HO Hydrogen Bonds and OH· · · OH (Dimer, Trimer, Oligomer) Hydrogen Bonds in PVA with 88% Saponification/PMMA and PVA with 99% Saponification/PMMA Blends and Their Thermal Behavior Studied by Infrared Spectroscopy. *Polymer* **2022**, *246*, 124725. [CrossRef]
56. Lee, D.H.; Song, Y.H.; Ahn, H.J.; Lee, J.; Woo, H.C. Fabrication and Characterization of Biopolymers Using Polyvinyl Alcohol and Cardanol-Based Polyols. *Molecules* **2024**, *29*, 4807. [CrossRef] [PubMed]
57. Ojha, S.; Ali, M.S.; Roy, M.; Bhattacharya, S. Hopping Frequency and Conductivity Relaxation of Promising Chalcogenides: AC Conductivity and Dielectric Relaxation Approaches. *Mater. Res. Express* **2021**, *8*, 085203. [CrossRef]
58. Lawaniya, S.D.; Awasthi, A.; Kuznetsova, I.; Kolesov, V.; Awasthi, K. Polymer Hybrid Based Nanomaterials for Next-Generation Sensing Technologies. *Sens. Actuators B Chem.* **2025**, *442*, 138162. [CrossRef]
59. Lew, T.T.S.; Sarojam, R.; Jang, I.-C.; Park, B.S.; Naqvi, N.I.; Wong, M.H.; Singh, G.P.; Ram, R.J.; Shoseyov, O.; Saito, K.; et al. Species-Independent Analytical Tools for next-Generation Agriculture. *Nat. Plants* **2020**, *6*, 1408–1417. [CrossRef] [PubMed]
60. Dicke, M.; Baldwin, I.T. The Evolutionary Context for Herbivore-Induced Plant Volatiles: Beyond the 'Cry for Help'. *Trends Plant Sci.* **2010**, *15*, 167–175. [CrossRef] [PubMed]
61. Yang, X.; Liu, X.; Zhao, N.; Chang, X.; Zheng, W.; Zhang, J. Beyond Conventional Sensing Paradigms: Multiscale Analysis of Conductivity-Type Switching in Semiconductor Gas Sensors. *Coord. Chem. Rev.* **2026**, *549*, 217286. [CrossRef]
62. Huang, L.; He, X.; Hu, J.; Qin, C.; Huang, C.; Tang, Y.; Zhong, F.; Kong, X.; Wei, X. Wearable Sensor Based on Covalent Organic Framework Humidity Films for Long-Term Monitoring of Tomato Physiology Under Abiotic Stress. *ACS Nano* **2024**, *18*, 33105–33118. [CrossRef] [PubMed]
63. Al-Ghamdi, A.A.; Algethami, N.; AlSulami, F.M.H.; Aldahiri, R.H.; Al-Sulami, A.I.; Alnawmasi, J.S.; Abdelrazek, E.M.; Farea, M.O.; Alqarni, M.A.; Alghamdi, H.M.; et al. Enhanced Structural, Optical, Dielectric, and Electrical Properties in Polymer Nanocomposite Films via Loading $AgNO_3$ NPs for Emerging Optical and Electrical Applications. *J. Mater. Sci. Mater. Electron.* **2024**, *35*, 1134. [CrossRef]
64. Zhang, R.; Wang, W.; Ge, Z.; Luo, C. Nonswellable and Highly Sensitive Hydrogel for Underwater Sensing. *J. Polym. Res.* **2024**, *32*, 4. [CrossRef]
65. Pi, M.; Qin, S.; Wen, S.; Wang, Z.; Wang, X.; Li, M.; Lu, H.; Meng, Q.; Cui, W.; Ran, R. Rapid Gelation of Tough and Anti-Swelling Hydrogels under Mild Conditions for Underwater Communication. *Adv. Funct. Mater.* **2023**, *33*, 2210188. [CrossRef]
66. Fan, Q.; Zhang, K.; Wei, L.; Gong, Y.; Qin, S.; He, M.; Liu, Y.; Luo, T.; Peng, S.; Yu, J. Molecular Weight Tailored Hydrogen Bonding Networks in PVA/PEDOT: PSS: Decoupling the Conductivity-Flexibility Trade-Off for Robust Epidermal EMG Monitoring. *ACS Appl. Mater. Interfaces* **2025**, *17*, 42278–42292. [CrossRef] [PubMed]
67. Li, Z.; Liu, Y.; Hossain, O.; Paul, R.; Yao, S.; Wu, S.; Ristaino, J.B.; Zhu, Y.; Wei, Q. Real-Time Monitoring of Plant Stresses via Chemiresistive Profiling of Leaf Volatiles by a Wearable Sensor. *Matter* **2021**, *4*, 2553–2570. [CrossRef]
68. Kwon, J.; Soh, J.-Y.; Shin, H.; Lim, S.; Yoon, S.Y.; Kim, W.-H.; Roh, D.-H.; Choi, M.; Park, S.-W.; Cho, E.; et al. Improving the Conductivity and Stability of Silver Nanowires Through Spontaneous Ligand Exchange for Joule Heating. *Angew. Chem. Int. Ed.* **2025**, *64*, e202518337. [CrossRef] [PubMed]
69. Kianpisheh, M.; Rezaei, B.; Babaei, Z.; Asadi, K.; Afshar-Taromi, F.; Sharifi Dehsari, H. Mechanically Stable Solution-Processed Transparent Conductive Electrodes for Optoelectronic Applications. *Synth. Met.* **2021**, *278*, 116805. [CrossRef]
70. Roh, H.; Kim, D.-H.; Cho, Y.; Jo, Y.-M.; del Alamo, J.A.; Kulik, H.J.; Dincă, M.; Gumyusenge, A. Robust Chemiresistive Behavior in Conductive Polymer/MOF Composites. *Adv. Mater.* **2024**, *36*, 2312382. [CrossRef] [PubMed]
71. Shrivastava, S.; Mahana, D.; Nehra, S.; Gangwar, S.; Singh, S.; Yadav, C.S.; Muthusamy, S.K.; Dogra, A. CO Gas Sensing Characteristics of $BaSnO_3$ Epitaxial Films Prepared by PLD: The Effect of Film Thickness. *Sens. Actuators B Chem.* **2024**, *400*, 134882. [CrossRef]
72. Nemufulwi, M.I.; Swart, H.C.; Mhlongo, G.H. Enhanced Propanol Response Behavior of $ZnFe_2O_4$ NP-Based Active Sensing Layer Induced by Film Thickness Optimization. *Processes* **2021**, *9*, 1791. [CrossRef]
73. Grossmann, L.; Duncan, D.A.; Jarvis, S.P.; Jones, R.G.; De, S.; Rosen, J.; Schmittel, M.; Heckl, W.M.; Björk, J.; Lackinger, M. Evolution of Adsorption Heights in the On-Surface Synthesis and Decoupling of Covalent Organic Networks on Ag(111) by Normal-Incidence X-Ray Standing Wave. *Nanoscale Horiz.* **2022**, *7*, 51–62. [CrossRef] [PubMed]
74. Chen, W.; Cnudde, P.; Van Speybroeck, V. Understanding the Entanglement between Diffusion and Reaction by Probing the Mobility of Ketene in Chabazites. *J. Catal.* **2026**, *453*, 116546. [CrossRef]

75. Almukhlifi, H.A.; Khasim, S.; Pasha, A. Fabrication and Testing of Low-Cost and Flexible Smart Sensors Based on Conductive PEDOT-PSS Nanocomposite Films for the Detection of Liquefied Petroleum Gas (LPG) at Room Temperature. *Mater. Chem. Phys.* **2021**, *263*, 124414. [CrossRef]
76. Deng, G.; Malola, S.; Yuan, P.; Liu, X.; Teo, B.K.; Häkkinen, H.; Zheng, N. Enhanced Surface Ligands Reactivity of Metal Clusters by Bulky Ligands for Controlling Optical and Chiral Properties. *Angew. Chem. Int. Ed.* **2021**, *60*, 12897–12903. [CrossRef] [PubMed]
77. Li, S.; Li, Y.; Wang, Y.; Pan, H.; Sun, J. Highly Stretchable, Elastic, Healable, and Ultra-Durable Polyvinyl Alcohol-Based Ionic Conductors Capable of Safe Disposal. *CCS Chem.* **2021**, *4*, 3170–3180. [CrossRef]
78. Li, W.; Jin, Y.; Song, P.; Cai, L.; Cao, X.; Elbugdady, I.; Hu, Z. Hygrothermal and Corrosive Effects on Mechanical Response and Fatigue Driven Cracking Behavior of Perfluorosulfonic Acid Ionomer. *Polymer* **2025**, *333*, 128678. [CrossRef]
79. Rodrigues, R.d.R.; Pellosi, D.S.; Louarn, G.; Péres, L.O. Nanocomposite Films of Silver Nanoparticles and Conjugated Copolymer in Natural and Nano-Form: Structural and Morphological Studies. *Materials* **2023**, *16*, 3663. [CrossRef] [PubMed]
80. Huang, L.; Tang, Y.; Liu, W.; Hu, Q.; Wei, X. Cellulose Paper-Based Humidity Power Generator with High Open Circuit Voltage Based on Zinc-Air Battery Structure. *Carbohydr. Polym.* **2024**, *326*, 121649. [CrossRef] [PubMed]
81. Mao, R.; Kishimoto, M.; Iwai, H. Multipoint Temperature Measurement Using Serially Connected Resistor–Capacitor Parallel Circuits by Impedance Spectroscopy. *Sens. Actuators A Phys.* **2021**, *331*, 113051. [CrossRef]
82. Duan, X.; Jiang, Y.; Liu, B.; Duan, Z.; Zhang, Y.; Yuan, Z.; Tai, H. Enhancing the Carbon Dioxide Sensing Performance of $LaFeO_3$ by Co Doping. *Sens. Actuators B Chem.* **2024**, *402*, 135136. [CrossRef]
83. Singh, A.; Ganapathysubramanian, B.; Singh, A.K.; Sarkar, S. Machine Learning for High-Throughput Stress Phenotyping in Plants. *Trends Plant Sci.* **2016**, *21*, 110–124. [CrossRef] [PubMed]
84. Kamilaris, A.; Prenafeta-Boldú, F.X. Deep Learning in Agriculture: A Survey. *Comput. Electron. Agric.* **2018**, *147*, 70–90. [CrossRef]

Disclaimer/Publisher's Note: The statements, opinions and data contained in all publications are solely those of the individual author(s) and contributor(s) and not of MDPI and/or the editor(s). MDPI and/or the editor(s) disclaim responsibility for any injury to people or property resulting from any ideas, methods, instructions or products referred to in the content.